Atomistic simulation of α-Al2O3 nanoparticle plastic anisotropy under compression

Qinqin Xu, Jérome Chevalier, Jonathan Amodeo

To cite this version:

Qinqin Xu, Jérome Chevalier, Jonathan Amodeo. Atomistic simulation of α-Al2O3 nanoparticle plastic anisotropy under compression. Journal of the American Ceramic Society, 2023, 10.1111/jace.19183 . hal-04171820

HAL Id: hal-04171820
https://hal.science/hal-04171820
Submitted on 28 Mar 2024

Originally published in Journal of the American Ceramic Society in 2023, cite as : Xu, Q., Chevalier, J., & Amodeo, J. (2023). Atomistic simulation of α-Al_2O_2 nanoparticle plastic anisotropy under compression. Journal of the American Ceramic Society, 106(10), 5986-5999. doi:`10.1111/jace.19183`

Atomistic simulation of α-Al_2O_3 nanoparticle plastic anisotropy under compression

Qinqin Xu,[1,2] Jérome Chevalier,[1] and Jonathan Amodeo[1,3,a)]

[1)] *Univ Lyon, CNRS, INSA Lyon, UCBL, MATEIS, UMR5510, Villeurbanne, 69621, France*

[2)] *National Centre for Nuclear Research, NOMATEN Centre of Excellence, Otwock, ul. A. Soltana 7, Poland*

[3)] *Aix-Marseille Université, Université de Toulon, CNRS, IM2NP, Marseille, 13013, France*

(Dated: 28 March 2024)

Alumina (α-Al_2O_3) is one of the major ceramic oxides commonly used for its advanced mechanical properties. Since recently, nanoscale α-Al_2O_3 requires more in-depth characterization related to ceramic powder compaction and sintering as well as for applications in the field of biomedical engineering. In this study, we use classical molecular dynamics simulations with a 2/3-body interatomic potential to investigate the mechanical response and the elementary deformation processes of α-Al_2O_3 nanoparticles under compression. Results show that α-Al_2O_3 nanoparticles resist up to particularly elevated critical force before yielding due to a surface nucleation process including various kinds of dislocations and nanotwins strongly sensitive to orientation and temperature. Results are rationalized in terms of stacking-fault energy and shear stress analysis and are discussed in the light of recent micromechanical tests as well as more fundamental observations performed in the bulk material.

[a)] Electronic mail: jonathan.amodeo@cnrs.fr

I. INTRODUCTION

α-alumina (α-Al_2O_3), also called sapphire or corundum, is one of the best-known oxide ceramics commonly used for its exciting mechanical properties in several fields of applications as medical engineering[1,2], abrasives[3,4] and catalysis[5,6]. Currently, various strategies are set up to further enhance the mechanical properties of alumina compounds including powder size refinement at the nanoscale with the aim to target alumina-based ceramics with submicron grain size after compaction and sintering[7]. Indeed and as for metals, reducing the size of single-crystalline ceramics deep in the submicron scale is known to promote the brittle-to-ductile transition and postpone (or inhibit) the brittle fracture process currently observed in ceramics single crystals[8–13]. Nevertheless, some questions remain about the plastic deformation mechanisms at the origin of such behaviour. Especially in the case of α-alumina where a better understanding of the stress response and elementary deformation processes might significantly help to better assess the fabrication of fine-grain samples.

In the bulk, the plastic deformation of sapphire is characterised by several slip systems including $\frac{1}{3}\langle 1\bar{2}10\rangle(0001)$ basal slip (c), prismatic $\frac{1}{3}\langle 1\bar{2}10\rangle\{10\bar{1}0\}$ (m) and $\frac{1}{3}\langle 10\bar{1}0\rangle\{1\bar{2}10\}$ (a) slip, rhombohedral slip $\frac{1}{3}\langle 0\bar{1}11\rangle\{01\bar{1}2\}$ (R) and various pyramidal and twinning slip systems. Several studies have focused on the deformation of bulk α-alumina, especially in an intermediate-to-high temperature regime where it shows high-strength and ductility[14–25]. Castaing and collaborators have investigated the mechanical properties of sapphire single crystals under compression for temperatures ranging from 25 to 1800°C[15]. Compression axis (CA) along the c axis or tilted 45° out lead to prismatic a (for T>200°C) and basal c (for T>600°C) slips, respectively. Also, Lagerlof *et al.* have characterized dislocation slip and twinning in sapphire using transmission electron microscopy (TEM)[19]. They observed prismatic a and m slip at temperatures as low as 200°C for CA along c while more complicated processes including basal and rhombohedral twinning are observed down to T=400°C for CA 45° off from $\left\langle 1\bar{2}10\right\rangle$. Basal slip was also observed in this second configuration but only at larger stresses. Pyramidal slip was characterized by Snow and collaborators in deformed polycrystalline alumina at 1150°C[26] while Geipel *et al.* have observed rhombohedral twins in α-Al_2O_3 single crystals for CA parallel to a $\langle\bar{2}110\rangle$ direction at 600°C. For this latter, the authors have identified screw twins with a $\left[0\bar{1}11\right]$ twin axis that involves shear along $\frac{1}{6}\left[0\bar{1}11\right]$ leading to a two-fold rotational symmetry[27]. Finally, He and collaborators have observed *c* and *R* twinning for CA along *a* and *m*, at temperatures of about 700-800°C confirming the sensitivity to orientation of the mechanical response of bulk sapphire[28].

Among the aforementioned slip processes occurring in bulk α-Al_2O_3, the basal edge dislocation is known to be one of the most common to appear during high-temperature deformation tests and has dragged a particular attention in the literature[17,19,24,29,30]. The $\frac{1}{3}\left\langle 1\bar{2}10\right\rangle$ perfect edge dislocation can dissociate into two partial dislocations with Burgers vectors $\frac{1}{3}\left\langle 10\bar{1}0\right\rangle$ and $\frac{1}{3}\left\langle 01\bar{1}0\right\rangle$. The dissociation process operates along a $\langle 0001\rangle$ direction via a climbing mechanism resulting into two mixed 60° dislocations[24]. Still, a net controversy persists about the partial dislocation core structures. Two main models were introduced to explain basal partial core structures and dislocation slip. On the one hand, Kronberg *et al.* proposed that partial dislocations can glide between two consecutive Al and O layers[31]. This slip model involves charge transport due to the strong bonding between Al and O atoms. But on the other hand, Bilde-Sørensen *et al.* proposed a mixed partial core that glides between two consecutive Al layers without charge transfer[32]. While Shibata *et al.* confirmed Kronberg's hypothesis using scanning electron microscopy (SEM)[30], Heuer *et al.* produced a markedly detailed atomic model of the dislocation cores with Al-Al terminated partial dislocations using the negative spherical-aberration imaging technique supporting the Bilde-Sørensen's model[24]. The Bilde-Sørensen mode was recently shown to be the more stable using atomistic simulations relying on fixed and variable charge models[33,34].

Montagne *et al.* studied the deformation processes of α-Al_2O_3 pillars using *in situ* SEM microcompression experiments at room temperature[35]. Four crystallographic orientations were investigated including m $\left[1\bar{1}00\right]$, a $\left[2\bar{1}\bar{1}0\right]$, R $\left[\bar{1}012\right]$ as well as c [0001]. The authors show that the deformation processes of α-Al_2O_3 micropillars depend on the orientation with multiple slip-systems involved including rhombohedral $\frac{1}{3}\langle\bar{1}101\rangle\{1\bar{1}02\}$ and $\frac{1}{3}\langle 0\bar{1}11\rangle\{0\bar{1}12\}$ as well as pyramidal $\frac{1}{3}\langle 0\bar{1}11\rangle\{1\bar{1}01\}$ slip systems. To improve the understanding of alumina mechanical properties at the nanoscale, Calvie *et al.* performed *in situ* TEM nanocompression tests of alumina nanoparticles (NPs)[36,37]. In particular, the authors emphasize the unprecedented ductility reached by the individual alumina nanocrystals although they do not conclude about the elementary mechanisms responsible for such critical behaviour.

Despite some recent micromechanical studies, the mechanical behavior of α-Al_2O_3 nanocrystals remains poorly documented and requires extensive characterization at the atomic scale. In this study, classical molecular dynamics (MD) simulations is used to investigate the mechanical properties and plasticity processes of α-Al_2O_3 nanoparticles under compression. In particular, the sensitivity of the stress response and elementary deformation processes to crystalline orientation and temperature is tested and discussed in the light of mechanical experiments performed at various scales.

II. SIMULATION METHODS

A. In silico design of neutral α-Al_2O_3 nanospheres

In this study, a pattern-based method is used for the design of α-Al_2O_3 nanoparticles with neutral surfaces. Basically, this method relies on the definition of neutral motives made of few atoms that are replicated on a 3D canvas designed *a priori* based on the target shape of the sample (Figure 1). Obviously, several motives and/or canvas can be used and the thinner the canvas *i.e.*, the smaller the motive, the more precise the sample surface discretization. One typical motive-canvas pair is the α-Al_2O_3 orthogonal unit-cell and its respective unit-cell lattice. While this guess is simple to build, it leads to particularly rough-shaped nano-objects when using it as a 3D pattern due to the large number of atoms (60 atoms) per unit cell.

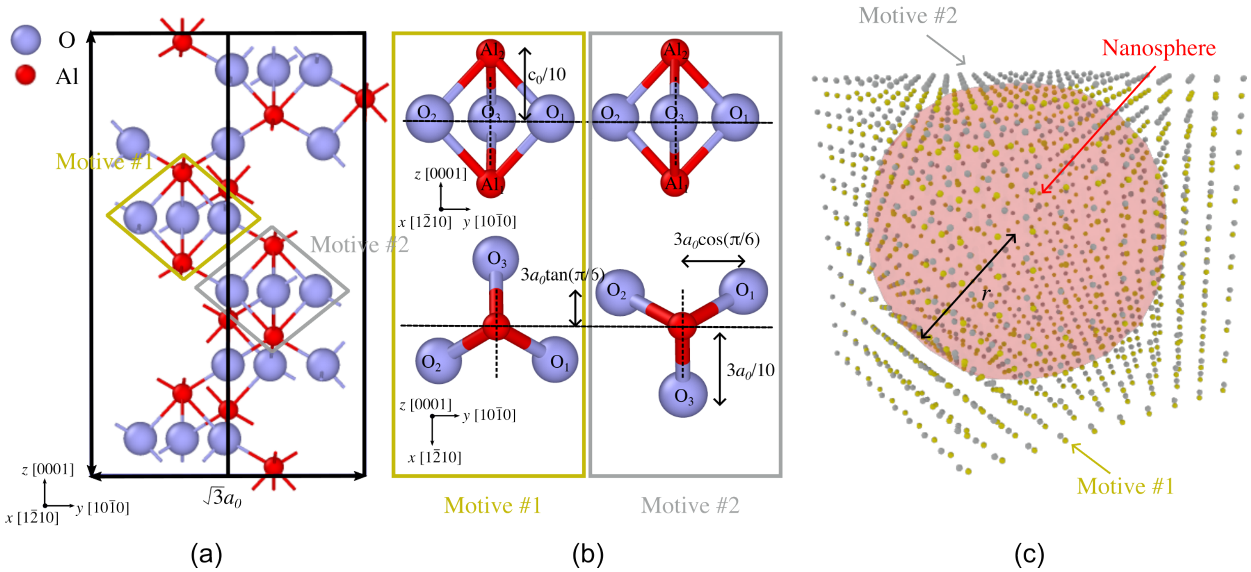

FIG. 1. Pattern-based method to construct α-Al_2O_3 neutral NPs. (a) α-Al_2O_3 partial unit cell with identification of the two motives to pattern, (b) *x* and *z* projections of both molecular motives, (c) 3D canvas made of replicated motives 1 and 2 from which the neutral nanosphere is carved out.

In this case, two motives made of a single α-Al_2O_3 molecule each (2×5 atoms) are used as shown Figure 1. The two motives differ only by their middle oxygen atom that alternates from a back-to-front x position. Assuming the origin of the motive at mid-distance between the two Al atoms, atoms of motive #1 are positioned at Al_1=(0,0,-$\frac{c_0}{10}$), Al_2=(0,0,$\frac{c_0}{10}$), O_1=($\frac{3a_0tan(\pi/6)}{10}$),$\frac{3a_0cos(\pi/6}{10}$,0), O_2=($\frac{3a_0tan(\pi/6)}{10}$,-$\frac{3a_0cos(\pi/6}{10}$,0) and O_3=(-$\frac{3a_0}{10}$,0,0). Motive #2 atom coordinates are easily derived from planar symmetry. These two motives are associated to two orthogonal canvas, namely canvas #1 and canvas #2, both oriented along x=[$1\bar{2}10$], y=[$10\bar{1}0$] and z=[0001] that allow the 3D mapping of whatever α-Al_2O_3 nano-object (particles, but also wires or thin films) with highly-discretized surfaces. Canvas #2 is shifted from canvas #1 by $\vec{t}$=(a_0, a_0.tan(π/6)/2,$-c_0$/6), both canvas grid coordinates are defined by Equation 1,

$$\begin{cases} c_{x(i,j,k)} = i.a_0 + j.a_0.cos(\pi/3) + k.a_0.cos(\pi/3) \\ c_{y(i,j,k)} = j.a_0.sin(\pi/3) + k.a_0.cos(\pi/3).tan(\pi/6) \\ c_{z(i,j,k)} = k.c_0/3 \end{cases} \tag{1}$$

where i, j and k are loop indices that allow the mapping of the entire 3D space. They correspond to the normalized coordinates of the both motive/canvas pairs. To build a neutral nanosphere, both canvas are truncated using the sphere definition $r^2 \geq (c_x - x_c)^2 + (c_y - y_c)^2 + (c_z - z_c)^2$ with (x_c, y_c, z_c) the coordinates of the sphere centre and r the nanoparticle radius.

B. Nanocompression

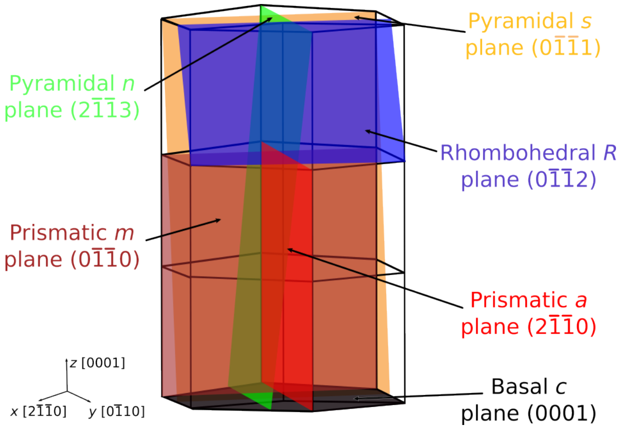

FIG. 2. α-Al_2O_3 hexagonal cell outlines and main crystallographic slip planes.

MD simulations are performed to investigate the deformation of α-Al_2O_3 NPs under compression using the open-source code LAMMPS[38]. All atomistic simulations are carried out using the 2/3-body Vashishta potential[39] that has recently shown to be particularly transferable to nanomechanics simulations as able to reproduce α-Al_2O_3 lattice, surface, stacking-fault and dislocations properties with good accuracy when compared to DFT and experiments[34]. A cut-off parameter for short-range interactions of 6 Å is used as in the original study of Vashishta and collaborators.

Neutral α-Al_2O_3 nanospheres with diameters ranging from 7.2 to 15.2 nm are investigated using CA normal to the *c*, *a*, *m* and *R* planes as illustrated in Figure 2. After NP building, the potential energy of the system is minimized using a force norm stopping criterion f_n=10^{-6} eV/Å. Then, two batches of samples are prepared. Both are heated up respectively to 600 and 1000 K using the canonical ensemble (NVT) and the Nosé-Hoover thermostat[40]. Then, NPs are equilibrated for 50 ps at constant temperature. After the equilibration process, the 600 K batch is cooled down to 5 K while the rest is saved aside for higher-temperature compression tests.

MD compression simulations are performed at 5 K and 1000 K using a displacement-controlled procedure developed by Amodeo and collaborators (see *e.g.*, Refs.[41–43]). After the NPs equilibration, nanocompression tests are performed using two infinite top and bottom force fields which behave respectively as a flat punch and a substrate. Both indenters are planar, axis-aligned and behave as infinitely-extent walls exerting forces of same amplitude but opposite directions on the NP. Non-periodic and shrink-wrapped boundary conditions are used. The total force F exerted by the indenter (or the substrate) on the NP is defined by $F = -K \sum_{j=1}^{N} (z_j - z_{ff})^2$, with K the force field constant set to 1000 eV/Å^3 for both the indenter and the substrate, z_j and z_{ff} respectively the atom j and force field z coordinate. K is imposed large enough to limit the penetration of both the indenter and the substrate into the NP. Within the LAMMPS fix-indent procedure, the moving indenter squeezes the NP and F applies to the atoms positioned over the indenter *i.e.,* the force is repulsive and becomes null if $z_j \leq z_{ff}$ (the reciprocal applies for the substrate force field).

Initial minimum and maximum atomic positions along CA are used to set the initial force field positions and reduce the rebound of the NP after contact. The position of the top indenter as function of time is computed as $P(t) = P_0(1 - \dot{\varepsilon}.n.dt)$ where P_0 is the starting position of the indenter, $\dot{\varepsilon}$ is the (engineering) strain rate, dt the timestep (1 fs) and n the number of elapsed simulation step. The indenter's displacement δ is recorded *on-the-fly* and an effective longitudinal strain $\varepsilon = \Delta L/D$ is defined as the ratio between the NP size variation ΔL in the CA direction and its original diameter D=$2r$. During compression, the top indenter is displaced at a constant displacement rate equivalent to $\dot{\varepsilon} = 10^8$ s^{-1} for all particle sizes, while the bottom indenter is kept fixed sustaining the sample.

In this study, the mechanical response of α-Al$_2$O$_3$ nanospheres is investigated for various CA orientations and the Hertz model $F(\delta) = \frac{4}{3}E^* r^{\frac{1}{2}} \delta^{\frac{3}{2}}$ where E^* is an effective Young's modulus and δ the cumulative displacement is used to characterize the force response within the elastic regime of deformation.

Elementary shear processes are investigated using the Dislocation Extraction Algorithm (DXA) here applied to the sole oxygen HCP sublattice and grain identification algorithm both available in Ovito[44,45]. Lee and Lagerlöf orientation table (provided in the Supplementary Materials) is also used to identify the angle θ between low-index crystalline planes in α-Al$_2$O$_3$ (as *e.g.,* the angle between CA and possible slip planes)[46]. θ can be computed using the three-index Miller notation (u, v, w) using the following equation,

$$cos(\theta) = \frac{a_0^2((u_1u_2 + v_1v_2) - 1/2(v_1u_2 + v_1u_2)) + c_0^2 w_1 w_2}{\sqrt{a_0^2(u_1^2 - v_1u_1 + v_1^2) + c_0^2 w_1^2}\sqrt{a_0^2(u_2^2 - v_2u_2 + v_2^2) + c_0^2 w_2^2}} \tag{2}$$

with the two crystallographic planes of interest defined by $(u_1, v_1, (t_1), w_1)$ and $(u_2, v_2, (t_2), w_2)$.

III. RESULTS

A. Orientation-dependent mechanical response of α-Al$_2$O$_3$ nanoparticle under compression

Figure 3 shows force *vs.* displacement curves for the various NP sizes, orientations and temperatures. All the samples are deformed up to ε=25% longitudinal strain. α-Al$_2$O$_3$ NPs under compression show an anisotropic mechanical response for which orientations can be ordered from the harder to the softer as $c > a > m > R$. In all the cases, the force response can be described using the usual two deformation regimes. At first, a reversible elastic regime is characterized by the slight ovalization of the nanosphere under compressive stress. The Hertz model particularly fits this first stage of the curves before theory and simulation diverged. At this stage, the force drop noticed on each curve relies on the withdrawal of the NP from the indenter due to the nucleation of dislocations (or nanotwins) from the contact surfaces between the force fields and the NP. Defect nucleation usually marks the initiation of the plastic deformation regime. In this latter, various

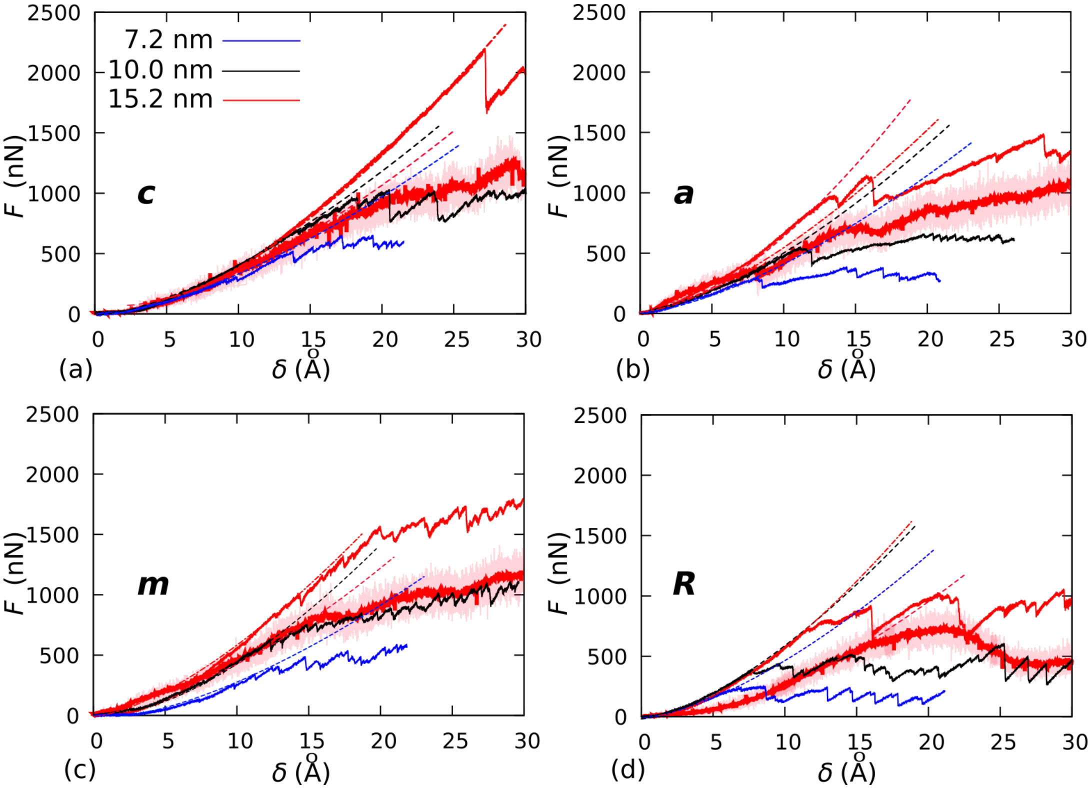

FIG. 3. Force *vs.* displacement curves for α-Al_2O_3 nanospheres under compression with compression axis normal to the (a) c, (b) a, (c) m and (d) R planes. Blue, black and red solid curves refer respectively to NP diameter D=7.2, 10.0 and 15.2 nm. The Hertz model is shown using dashed curves. Simulations are performed at T=5 K (thin curves) for the three diameter sizes except for D=15.2 nm for which additional T=1000 K data (thicker curves) are shown. For this latter, raw data are shown blurred while a Bezier fit is highlighted.

kinds of dislocation-based processes occur in the simulations depending on the orientation, this will be the subject of the next section. Overall, reducing the NP size reduces the force range required to deform the system due to the reduction of the amount of atoms N contacting with the indenter. One can note that the compressive stress (F/S where S is the instant contact surface computed *on-the-fly*) might show the opposite trend, S generally decreasing even more when reducing the particle size (see discussion in Ref.[42]). Increasing the temperature also has a softening impact as shown by the additional simulations performed at 1000 K, as usually observed in bulk alumina[19,47–49].

Table I resumes the effective Young's modulus E^* and the fitting interval $[E^*]$, as well as criti-

TABLE I. Mechanical response of α-Al_2O_3 nanosphere under compression as function of orientation (CA) and size (D) at T=5 K. Effective Young's modulus E^*, fitting intervals [E^*] and critical data for dislocation or twin nucleation including critical force F_c, displacement δ_c and strain ε_c. Additional data for T=1000 K are shown between braces for D=15.2 nm NPs.

CA	D [nm]	E^* [GPa]	[E^*] [Å]-[Å]	F_c [nN]	δ_c [Å]	% ε_c [-]
	7.2	167.0	2.5-9.0	286.0	9.0	12.5
c	10.0	190.0	3.5-13.0	943.0	18.1	18.1
	15.2	191.0 (127.0)	7.6-27.0 (1.5-14.3)	1000.0 (400.0)	17.3 (17.3)	11.5 (5.4)
	7.2	237.0	1.8-5.0	287.0	8.0	11.1
a	10.0	220.0	1.5-7.0	538.0	11.1	11.1
	15.2	239.0 (154.0)	1.5-13.7 (0.8-4.2)	550.0 (380.0)	9.0 (8.5)	6.0 (6.0)
	7.2	189.0	3.6-6.5	270.0	7.1	9.8
m	10.0	195.0	6.0-11.0	624.0	12.3	12.3
	15.2	203.0 (157.0)	7.6-12.9 (3.0-16.7)	810.0 (820.0)	12.9 (16.3)	8.5 (10.7)
	7.2	258.0	1.1-5.4	241.0	6.8	9.4
R	10.0	247.0	1.0-8.0	391.0	7.8	7.8
	15.2	248.0 (111.0)	0.8-11.9 (4.6-14.7)	720.0 (722.0)	11.9 (20.8)	7.8 (13.7)

cal force F_c, displacement δ_c and strain ε_c for the nucleation of defects characteristic of the plastic deformation regime and computed from the MD simulations as a function of size, orientation and temperature. Results show that the largest yield force is obtained for CA normal to the *c* plane at low temperature, while the *m* and *R* orientations are stronger at high temperature, both being less impacted by the temperature increase when compared to the *c* and *a* orientations. It is worth noticing that E^* should not be compared to bulk-alumina Young's modulus due to the heterogeneous stress state of the nanosphere under compression (see Ref.[50] for a detailed discussion) but one can emphasize that it is already four times larger than in the case of Al nanospheres of comparable size (10 nm, E^*=45.9 GPa)[51].

B. Elementary deformation processes

The following section focuses on describing the elementary plastic deformation processes that occur in α-Al_2O_3 NP under compression as a function of the orientation. No size-effect on the plastic deformation processes was noticed in the investigated dimension range. Therefore, most of the detailed analysis presented in the following will only focus on the D=15.2 nm NP at T=5 K for the sake of consistency. The influence of temperature on the dislocation-based mechanisms are discussed in the last section.

1. *Compression axis normal to the c plane*

When compressed along the c axis, the first non-elastic event in the 15.2 nm NP occurs at ε = 11.5% (δ=17.5 Å) and a loading force F_c=1000 nN. Atomic planes stacking and crystal analysis confirm the nucleation of a nanotwin (Figure 4) correlated to a slip plane deviation of about 58° from CA what suggests a $(01\bar{1}2)$ rhombohedral nanotwin when referring to the Lee and Lagerlof table[22,27]. The θ=58° angle is confirmed when applying Equation 2 to $(01\bar{1}2)$ using an inverse approach. The nanotwin nucleates from the contact region between the substrate and the NP as shown in Figure 4a. In contrast to the classical twin growth scheme depicted in α-Al_2O_3 by Kuksin[52], here we did not observe the prior nucleation of a partial dislocation (further growing into a twin) but directly an already-shaped *volumic* defect. The DXA analysis suggests a $[0\bar{1}11]$ Burgers vector for identified disconnections. After nucleation, the nanotwin only propagates to a limited extent within the sample what explains the continuous increase of the force recorded *i.e.,* no force drop is observed on the mechanical response at this stage (Figure 3a, thin red curve).
Thus, the elastic regime continues up to 17.8% (δ=27.0 Å) where a more pronounced transition to the plastic regime is emphasized by a significant force drop on the curve. At this stage, a second rhombohedral twin is nucleated within the same slip plane but in the opposite gliding direction *i.e.,* from the top indenter contact region, as shown in Figure 4b. This new nanotwin quickly propagates through the entire particle forming new Twin Boundaries (TB) that extent to the NP surface for the first time. The two parallel *R* twins are spaced from each other and twin growth is observed thanks to successive nucleation and glide events on neighboring $(01\bar{1}2)$ planes leading to the TB migration. At ε = 17.9% (δ=27.1 Å), a third rhombohedral twin suddenly forms in the $(1\bar{1}02)$

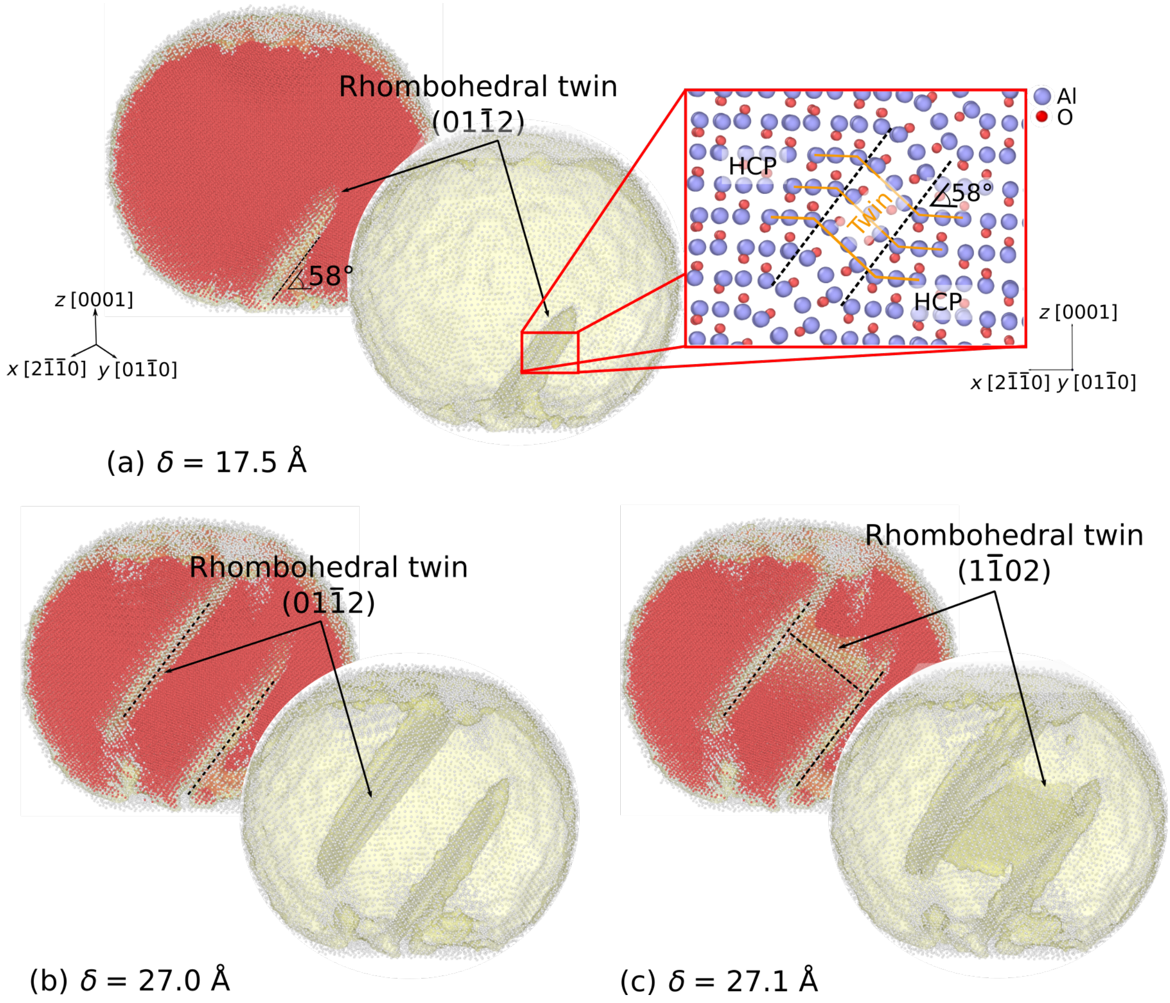

(a) δ = 17.5 Å

(b) δ = 27.0 Å

(c) δ = 27.1 Å

FIG. 4. Nucleation of rhombohedral twins in a 15.2 nm α-Al_2O_3 NP under compression along the *c* plane. Displacements (a) δ=17.5 Å, (b) δ=27.0 Å and (c) δ=27.1 Å are shown. An angle of 58° is measured between the first twinning plane and the *c* plane. Nanoparticle cross-sections are illustrated with (back figures) and without (front figures) perfect crystal atoms to emphasize the presence of defects. Only O atoms are shown for the sake of clarity. They are colored in red or light-grey depending on the local crystal structure *i.e.,* respectively when they belong to the HCP perfect crystal environment or defective regions (surfaces or twin boundaries). Grain and twin boundary interfaces are colored in yellow. In the top-right inset, both O and Al atom sublattices are shown respectively in blue and red.

slip plane and intersects with the first two parallel twins (Figures 4c). Increasing compression, the third twin creates junctions between existing TBs and the NP surfaces.

2. Compression axis normal to the a plane

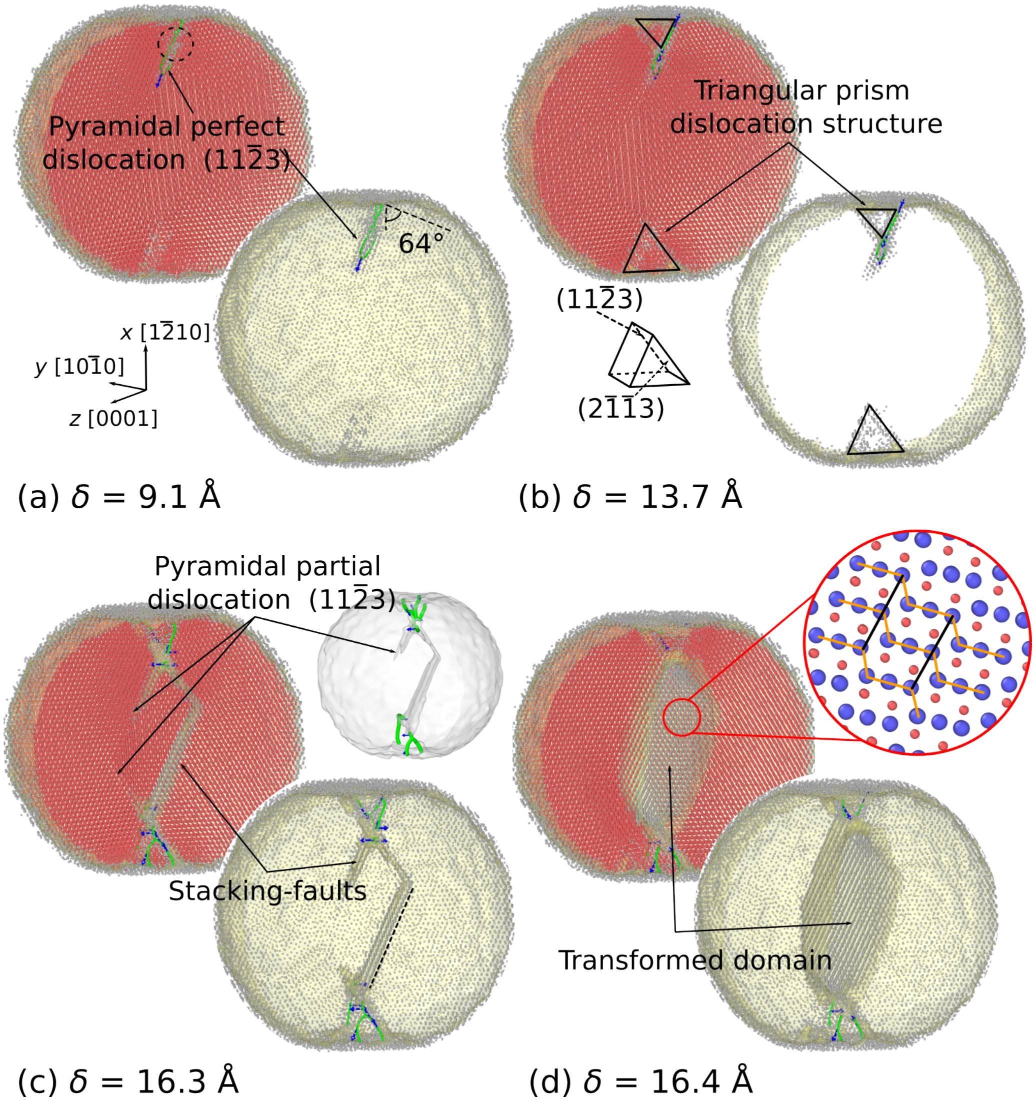

FIG. 5. Compression of α-Al$_2$O$_3$ NPs normal to the prism a plane. (a) δ=9.1 Å, nucleation and propagation of a perfect $(11\bar{2}3)$ pyramidal dislocation, (b) δ=13.7 Å, formation of a triangular structure made of perfect dislocations gliding in $(11\bar{2}3)$ and $(2\bar{1}\bar{1}3)$. (c) δ=16.3 Å, the triangular dislocation structure fails and partial dislocations multiply within same pyramidal slip planes. Staking-faults are emphasized using yellow interfaces in the main figure, light-grey one in the inset. (d) δ=16.4 Å, the accumulation of closed stacking-faults in the pyramidal planes lead to structural change in the central part of the NP. Additional information are provided in the caption of the Figure 4. In addition, the local crystallographic structure of the transformed domain is illustrated in the inset, perfect dislocations are shown in green while Burgers vectors are shown using blue arrows.

Plastic deformation processes are different for CA normal to the *a* plane as simulation does now show any twinning. In this case, the first plastic deformation event happens in the largest sample at ε = 6.0% strain (δ=9.1 Å) and a loading force F about 550 nN (Figure 3b). At this stage, a perfect dislocation nucleates from the top region of the NP, as shown Figure 5a. The atomic configuration in the vicinity of the pyramidal dislocation core is highly disordered as also observed by Zhang *et al.*[53] using the same interatomic potential. The dislocation propagates within a slip plane oriented at 64° from CA, in line with the $(11\bar{2}3)$ pyramidal *n* plane suggested by the Lee and Lagerlof table. Here again the dislocation quickly stops gliding after nucleation what explains the lack of force drop on the mechanical response, as in the case of the basal compression test. The first load drop is observed at ε = 9.0% (δ=13.7 Å, Figure 5b) where two $(11\bar{2}3)$ and $(1\bar{2}13)$ pyramidal dislocations nucleate from the NP bottom region making a triangular prism dislocation structure, in a similar manner than the pyramidal dislocation structure observed in FCC metals[51,54,55]. While the compression proceeds an other prism structure forms in the bottom part of the NP and then, a second force drop of larger amplitude is observed at ε = 10.6% (δ=16.1 Å) that is attributed to the propagation of a new pyramidal dislocations from the hillock of the triangle structure (Figure 5b and c). These dislocations are of different types with respect to the perfect one of Figure 5a. Indeed, they are partial dislocations followed by stacking-faults. The prism structures definitely break at ε = 10.7% (δ=16.3 Å) where multiple partial dislocations propagate in close and parallel slip planes. Finally, the propagation of the pyramidal partial dislocations leads to a crystallographic structural change between the lateral and central domains of the NP made of stacking-fault every tow planes, as shown in Figure 5d. A similar substructure made of stacking-faults every two planes was already observed in intermetallic NPs[56].

3. *Compression axis normal to the m plane*

When compressing perpendicularly to the *m* plane, the first nucleation event in the largest sample happens at ε = 8.5% (δ=12.9 Å) and at a loading force about F=810 nN (Figure 3c). Few partial dislocations with Burgers vectors of type $\frac{1}{3}[10\bar{1}0]$ nucleate and propagate in the *c* plane (see Figure 6). One can note that, originally, the *c* plane is supposed to be perpendicular to CA (leading the a null Schmid factor) but basal slip is here activated due to a slight rotation of the NP happening at the beginning of the compression (see Figure 6a). Dislocations nucleate from the two contact regions and plasticity is extremely localized in this case, as shown in Figure 6b and c *i.e.,* several partial dislocations nucleate in planes separated of 2 or 4 interplanar distances (without generating nanotwin). In this case, no clear force drop is noticed on the mechanical response but only low-amplitude variations superimposed to an overall strain-hardening behaviour. These hits are attributed to further nucleation events that contradict the basal dislocations propagation which is already impeded by the low-Schmid factor orientation. Indeed, one can notice some plastic activity starting from ε = 11.5% (δ=17.5 Å) in an other slip plane including several dislocation nucleation events that happen in a similar manner that in the aforementioned *a* case *i.e.,* partial dislocations in close planes, as shown Figure 6c. The activated slip plane makes an angle of 65° with CA which suggests a rhombohedral *R* plane following Lee and Lagerlof (owing the initial rotation of the NP). Between 11.5% (δ=17.5 Å) and 20% (δ=30.0 Å), both slip systems compete together with plasticity strictly localized in the both indenter and substrate regions. No propagation of dislocation is observed in the central domain of the NP assuming (i) a hard-orientation, unfavourable to plastic deformation (ii) strong deformation heterogeneities and (iii) a larger elastic strain contribution to the total strain that is specific to the *m* orientation.

4. *Compression axis normal to the R plane*

As shown Figure 7, the first nucleation event in the 15.2 nm NP when compressed perpendicularly the $(10\bar{1}2)$ *R* plane occurs at ε=7.8% (δ=11.9 Å). At this stage, a $\frac{1}{3}[01\bar{1}0](0001)$ leading partial dislocation nucleates from the contact region between the substrate and the NP as shown Figure 7a. It is quickly followed by the $\frac{1}{3}[10\bar{1}0](0001)$ trailing partial dislocation leading to the dissociated $\frac{1}{3}[1\bar{2}10]$ dislocation in the basal plane (Figure 7a). In this case, the gliding plane is positioned between two puckered Al layers as in the Bilde-Sørensen model for the basal edge dislocation[32]. After ε=7.8% (δ=11.9 Å), several paralleled basal dislocations with similar Burger vectors nucleate from the contact regions of the NP with the indenter and the substrate. Those dislocations often cross-slip towards adjacent basal planes. Few $(11\bar{2}3)$ pyramidal (perfect) dislocations are also observed (Figure 7b). They are always connected to a basal dislocation and are generated by the cross-slip of screw segments. At larger strain, structural changes associated to the glide of multiple pyramidal partial dislocations are observed similarly to the prism *a* case (Figure 5).

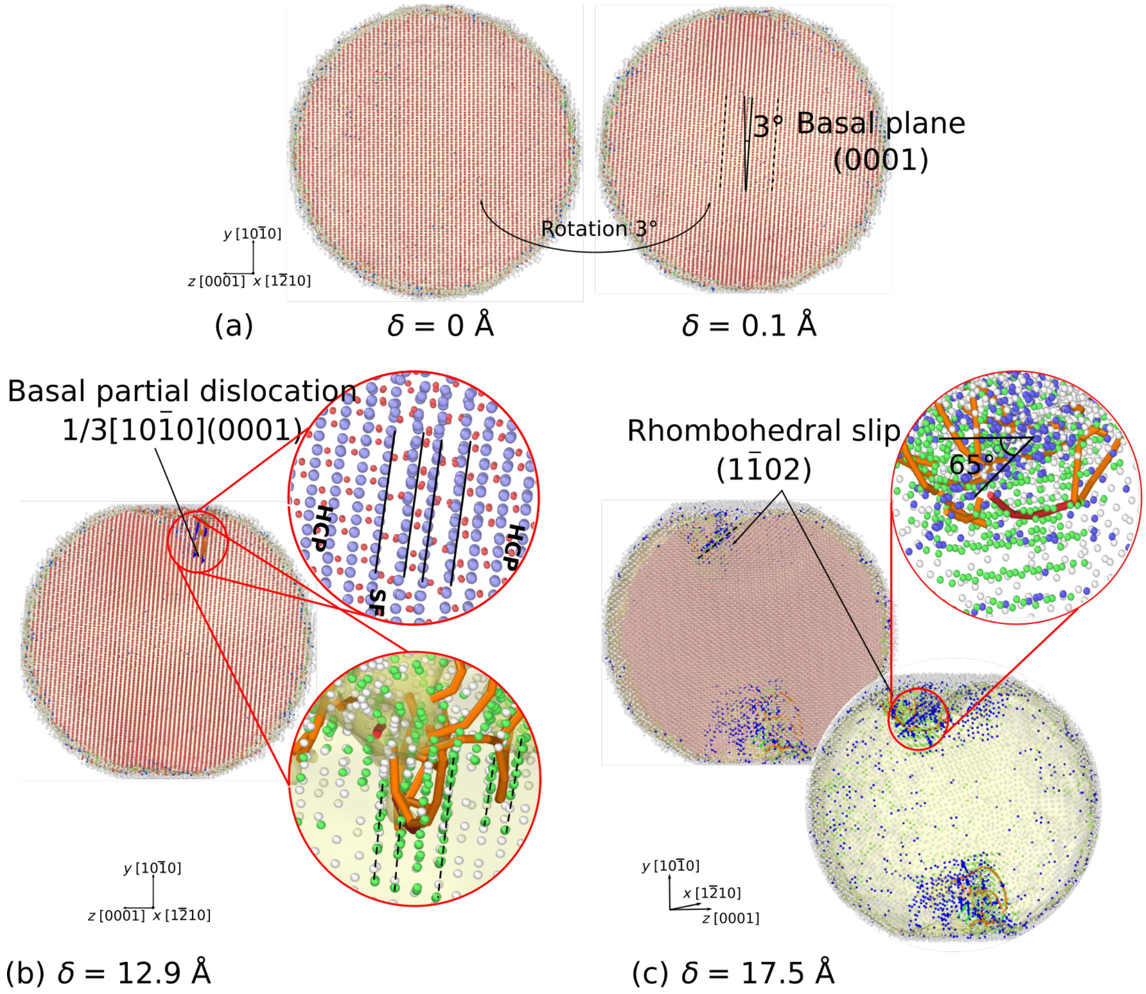

FIG. 6. Compression of α-Al$_2$O$_3$ NPs normal to the prism *m* plane. (a) up to δ=0.1 Å, the NP rotates to accommodate the deformation and the basal plane is tilted of about 3° from CA, (b) δ=12.9 Å, basal partial dislocations nucleate from the contact region with the indenter. Dislocations colored in orange refer to $\frac{1}{3}[10\bar{1}0]$ dislocations (atoms colored in green rely to the stacking-faults). (c) δ=17.5 Å, dislocations nucleate in the rhombohedral $(1\bar{1}02)$ slip system at 65° from the compression axis and interact with basal dislocations. Additional information are provided in the caption of the Figure 4.

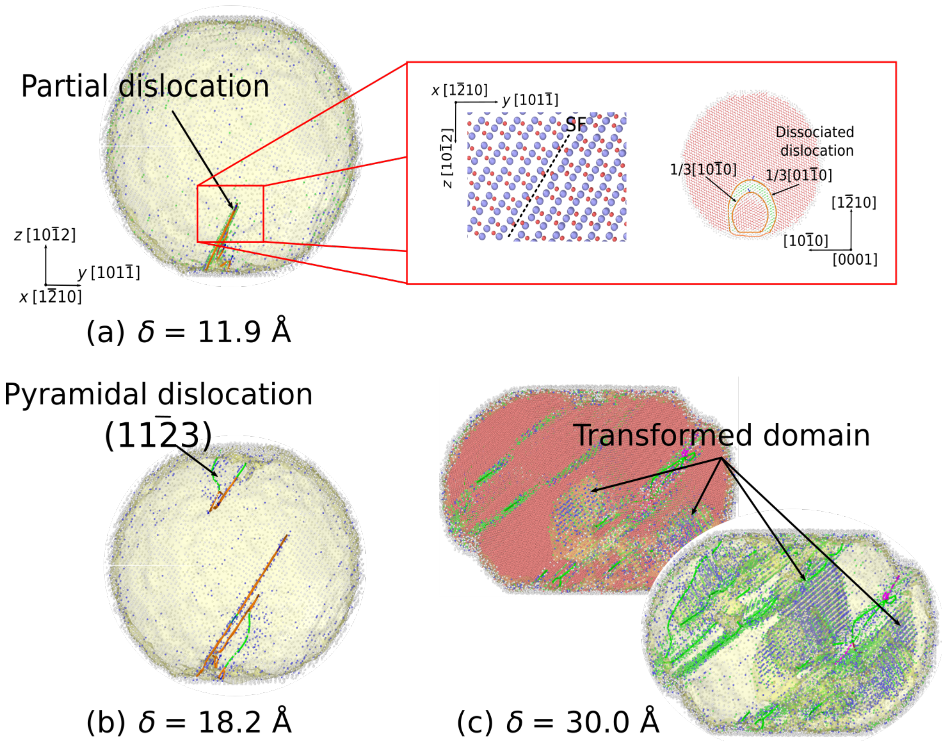

(a) δ = 11.9 Å

(b) δ = 18.2 Å

(c) δ = 30.0 Å

FIG. 7. Compression of α-Al_2O_3 NP with CA normal to a rhombohedral R plane. (a) δ=11.9 Å, nucleation of dissociated dislocations in the c plane. Partial dislocations are colored in orange, stacking fault atoms in green, (b) δ=18.2 Å, basal (colored in orange) and pyramidal (colored in green) dislocations nucleating and propagating, (c) δ=30.0 Å, basal partial dislocations gliding in planes close to transformed domains associated to the propagation of pyramidal n partial dislocations (stacking-fault atoms colored in blue). Additional information are provided in the caption of the Figure 4.

IV. DISCUSSION

A. Orientation dependence and plastic anisotropy

Our results show that the slip system activity in α-Al_2O_3 NPs strongly depends on the CA orientation and temperature with significant variations of the yield force F_c. Table I shows that the largest yield force F_y is obtained when CA is normal to the c plane. This result is in good agreement with the study of Montagne *et al.* that performed *in situ* SEM tests on alumina micropillars at room temperature[35]. For CA normal to the c and m planes, Montagne and colleagues characterized R slip which is confirmed by our MD simulations on NPs at low temperature for which (i) R twinning is observed for CA normal to the c plane and (ii) R slip in addition to c slip are shown for CA normal to the *m* plane. Both studies also show pyramidal slip when CA normal to an *a* plane but in different slip planes *i.e.,* the *s* $\{1\bar{1}01\}$ is observed by Montagne *et al.* while the *n* $\{2\bar{1}\bar{1}3\}$ is dominant in our case. Finally, Montagne *et al.* did not observed plasticity when compressing micropillars with CA axis-aligned with the *R* normal while MD simulations show *c* and pyramidal slip at low temperature. We believe that this could be attributed to a size-effects *i.e.,* nanoscale samples are less likely to break when compared to larger micropillars. Overall, this comparison confirms the robustness of the Vashishta interatomic potentials to model the various deformation processes occuring in α-alumina.

In the following, Schmid factor and stacking-fault energy (SFE) analyses are performed to interpret the plastic anisotropy observed in the simulation. The Schmid factor *M* is commonly used to translate an applied compressive stress σ into a shear stress $\tau = M.\sigma$ with $M = cos(\phi).cos(\lambda)$, ϕ and λ being the angles made by the CA direction $\vec{s}$ with the slip plane normal $\vec{n}$ and the Burgers vector $\vec{b}$, respectively. As described *e.g.*, by Zhang *et al.*[57], $\vec{n}$=$[u_1 = (2h_1+k_1), v_1 = (h_1+2k_1), w_1 = \frac{3l_1}{2}(\frac{a_0}{c_0})^2]$, $\vec{s}$=$[u_2 = (h_2-m_2), v_2 = (k_2-m_2), v_2 = l_2]$ and $\vec{b}$=$[u_3 = (h_3-m_3), v_3 = (k_3-m_3), v_3 = l_3]$ using the 3 Miller indices notation [h,k,l]. Thus, cos(ϕ) and cos(λ) are defined as,

$$\begin{cases} \cos\phi = \dfrac{\left[u_1u_2+v_1v_2-\frac{1}{2}(u_1v_2+u_2v_1)+\left(\frac{c_0}{a_0}\right)^2 w_1w_2\right]}{\left[(u_1^2+v_1^2-u_1v_1+\left(\frac{c_0}{a_0}\right)^2 w_1^2)\left(u_2^2+v_2^2-u_2v_2+\left(\frac{c_0}{a_0}\right)^2 w_2^2\right)\right]^{\frac{1}{2}}} \\ \cos\lambda = \dfrac{\left[u_3u_2+v_3v_2-\frac{1}{2}(u_3v_2+u_2v_3)+\left(\frac{c_0}{a_0}\right)^2 w_3w_2\right]}{\left[(u_3^2+v_3^2-u_1v_3+\left(\frac{c_0}{a_0}\right)^2 w_3^2)\left(u_2^2+v_2^2-u_2v_2+\left(\frac{c_0}{a_0}\right)^2 w_2^2\right)\right]^{\frac{1}{2}}} \end{cases} \tag{3}$$

In the following, we use literature observations[19,26,35,58–60] as well as γ-lines computed using the same Vashishta potential to identify the possible partial and perfect Burgers vector directions for each slip system. Parts of the γ-lines were already introduced in Ref.[34]. Outcomes are resumed in Table II.

Owing the large amount of available slip systems in α-Al_2O_3 (about 30 without considering partial dislocation slip systems), only main slip systems including those observed in experimental studies and in our simulations are discussed in the following. γ-lines of interest computed using the Vashishta potential are shown in Figure 8. Each orientation is discussed in the following.

TABLE II. Schmid factor analysis as function of compression orientation and slip system in α-Al_2O_3. $\vec{b}_p$ refers for (leading or trailing) partial dislocation Burgers vector while $\vec{b}$ relies on perfect Burgers vectors. M and M_p refer respectively to perfect and partial systems Schmid factors.

Slip plane		Burgers vector		Compression orientation							
				c		a		m		R	
		$\vec{b}$	$\vec{b}_p$	M	M_p	M	M_p	M	M_p	M	M_p
Basal c	(0001)	$\frac{1}{3}\langle 1\bar{2}10\rangle$	$\frac{1}{3}\langle 1\bar{1}00\rangle$	0.00		0.00		0.00		0.25	0.28
Prismatic a	$\{1\bar{2}10\}$	$\langle 10\bar{1}0\rangle$	$\frac{1}{3}\langle 10\bar{1}0\rangle$	0.00		0.43		0.43		0.04	
Prismatic m	$\{10\bar{1}0\}$	$\frac{1}{3}\langle 1\bar{2}10\rangle$		0.00		0.43		0.43		0.04	
Rhombohedral R	$\{0\bar{1}12\}$	$\frac{1}{3}\langle 0\bar{1}11\rangle$	$\frac{1}{6}\langle \bar{2}021\rangle$	0.45	0.33	0.34	0.50	0.45	0.33	0.46	0.45
Pyramidal n	$\{11\bar{2}3\}$	$\frac{1}{3}\langle \bar{1}101\rangle,\langle 10\bar{1}0\rangle$		0.40, 0.00		0.20, 0.38		0.20, 0.38		0.50, 0.03	
Pyramidal s	$\{1\bar{1}01\}$	$\frac{1}{3}\langle 1\bar{1}01\rangle$		0.25		0.38		0.38		0.03	

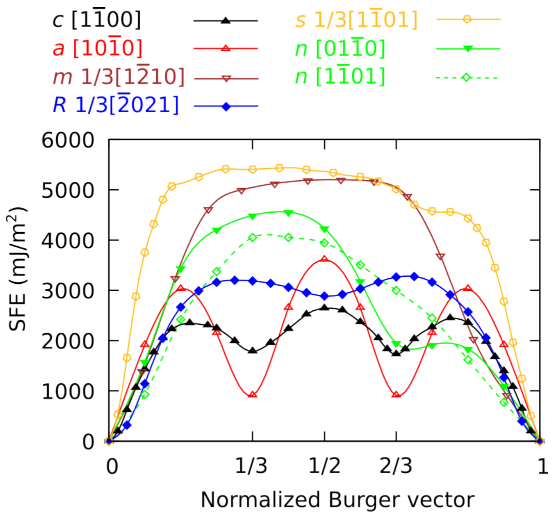

FIG. 8. Stacking-fault energy (SFE) profiles in c, a, m, n, s and R slip planes computed using the Vashishta interatomic potentials. Profile directions corresponding to Burgers vectors are provided in the legend.

1. ***Compression normal to the c plane*** (0001)

Table II shows Schmid factors as computed using Equation 3 for R, n and s slip systems. For the c orientation, Schmid factor in c, m and a slip systems (partial and perfect) are null. Thus, this orientation is more prone to rhombohedral and pyramidal slips. Indeed, the rhombohedral slip planes $(01\bar{1}2)$ and $(1\bar{1}02)$ show a high Schmid factor for the perfect dislocation slip system M=0.45 and a slightly lower one for partial slip system M_p=0.33 (for both the leading and the trailing partial dislocation). Owing the high-energy barriers for full-Burgers vector translation in the R slip system (see Figure 8) and the length of respective Burgers vectors, partial slip or twinning in the R plane might be favoured at elevated stress for this specific orientation as shown by Sarobol *et al.* using microscropy and MD nanocompression[58]. Based on the γ-line analysis, pyramidal n slip systems rely on perfect $\frac{1}{3}\langle\bar{1}101\rangle$ and $\langle 01\bar{1}0\rangle$ perfect (or partial) Burgers vectors (dissociation in n slip system has however never been discussed in the literature). While Schmid factor is null in the latter for CA along the c axis, the γ-line for $\langle\bar{1}101\rangle$ shows a single-hump profile with elevated energy. The same high-energy barrier is noticed for the s slip systems with in addition a lower Schmid factor (M=0.25). These analyses justify the occurrence of R twins in our simulations when NPs are deformed along c. One can note that only R perfect dislocations (no twin) were characterized by Montagne *et al.* in *in situ* SEM micropillar experiments possibly due to the lower stress reached in the experiment induced by larger size samples (size-effect). Finally, the occurrence of R twins for CA along [0001] is also in agreement with compression experiments performed in bulk α-Al_2O_3 at 800°C by Lagerlof *et al.*[19].

Compression normal to the a plane $\{1\bar{2}10\}$

Schmid factors for the various c and a slip systems (including partial slip systems) as well as those relying on the $(10\bar{1}2)$ R plane are null when compressing perpendicularly to the a plane. Nevertheless, several slip systems remain available including m, R and presumably pyramidal n slip systems. Only one of the two partial slip systems has a non-zero Schmid factors within the $(01\bar{1}2)$ and $(1\bar{1}02)$ slip planes what might not favour R partial slip or twinning. On the other hand, prism m has a high Schmid factor (M=0.43) but a very unlikely energy profile as shown in Figure 8. Nanocompression simulations along the a direction show dislocation nucleation in symmetric n planes $(11\bar{2}3)$ and $(2\bar{1}\bar{1}3)$ that further dissociate (see Figure 5). These observations are in good agreement with Kim *et al.* MD nanoindentation for the same orientation[59]. This coincides with the moderate Schmid factor values and SFE profiles computed for the two representative Burgers vectors in the n slip system. While the competition between n and R slip is obvious in this case, the absence of a slip is surprising as stable SFE in the a slip plane is quite low. We assume that this absence is justified by the length of the Burgers vector in the *a* slip system that is larger than 8 Å when compared to the shorter one in *R* and pyramidal *n* slip systems, as confirmed by Snow *et al.*[26]. However, It is worthy to point out that while pyramidal slip was also characterized in Montagne *et al.* micropillar experiments for this orientation, only pyramidal *s* that shows unfavorable energy profile in Figure 8 was concerned and not pyramidal *n*.

Compression normal to the m plane $\{10\bar{1}0\}$

Table II shows Schmid factors for the various slip systems with CA along the $[10\bar{1}0]$ direction. Perfect $[0\bar{1}10](\bar{2}110)$ and $[\bar{1}100](11\bar{2}0)$ prism *a* as well as the $[10\bar{1}1](10\bar{1}2)$ *R* slip systems exhibit particularly high Schmid factors with M=0.43, 0.43 and 0.38, respectively. Other *R* slip systems exhibit lower values while the remaining *m* slip system has a null Schmid factor for the tested CA. Two configurations are noticed for partial *R* slip systems including (i) M_p=0.33 and 0.17 alternatively, respectively for leading and/or trailing partial dislocations and (ii) M_p=0.43 and 0.33 for the leading and trailing partial dislocations, respectively. Only dissociation in the $(10\bar{1}2)$ slip plane leads to the second configuration. In the low-temperature simulation, we observe partial dislocations in the *R* slip system in agreement with the Schmid hypothesis in addition to basal slip which is associated to a rotation of the NP in the initial stage of the compression. Kim *et al.*[61] also observed *R* slip for this orientation in MD simulation just like Montagne *et al.* in their alumina micropillar compression tests. Finally, the occurrence of *R* partial dislocation and twins is also in agreement with observations performed in bulk when compressed along $[10\bar{1}0]$[19,28].

Compression normal to the R plane $\{10\bar{1}2\}$

The *R* case is the one leading to the more widespread Schmid factor distribution including possible slip in various perfect and partial slip systems (Table II). Indeed, *c* (perfect and partial), *R* (perfect and partial) and pyramidal *n* slip systems might be activated while all *m* and *a* slip systems show nearly zero Schmid factor (M<0.1). More precisely, the two $[11\bar{2}0](0001)$ and $[\bar{2}110](0001)$ perfect *c* slip systems have M=0.25 (the last one being null), while respective partial slip systems show M_p=0.28 and 0.14 (or 0.14 and 0.28), the third dissociated slip systems is characterized by lower Schmid values (M_p=0.14 for both leading and trailing partial dislocations) while its perfect counterpart has a null Schmid factor. Assuming the low-energy of the basal SFE profile, basal slip might be favoured in this case. However, R and n slip systems also show high Schmid factors. Two over three R planes are characterized by M=0.46 and M_p=0.23, 0.45 while the last one is characterized by M=0.24 and M_p=0.18 for both partial dislocations. Finally, both pyramidal n slip systems are characterized by M=0.50 and M_p=0.10, 0.03 respectively for Burgers vector along $\langle\bar{1}101\rangle$ and $\langle 10\bar{1}0\rangle$.

Again, the Schmid and SFE analyses explain the observations made out of the simulation. Indeed, c slip is observed whatever the temperature due to its particularly low SFE while pyramidal n is also observed (especially at low temperature), probably due to a particularly high Schmid factor. Same slip systems were observed in Kim *et al.* MD nanoindentation simulations[59]. However, it can be noticed that only cracks (no slip) were characterized by Montagne *et al.* in *in situ* SEM compression micropillar[35] probably because of to the larger sample tested by the authors.

B. On the effect of temperature

Temperature influences the mechanical behaviour and activated slip systems in α-Al_2O_3 NPs. Force *vs.* displacement curves computed at T=1000 K show more noise due to the increase of atomic vibrations and their consequences on the indenter force calculation. They are also soften in both the elastic and plastic regimes (see Figure 3) and both the yield force F_y and effective Young's modulus drop down when increasing T (see Table I). This behaviour is in good agreement with what is known from bulk alumina[19]. Maximum $\langle E^* \rangle$ is noticed for the $\left[10\bar{1}2\right]$ orientation at 5 K while it is $\left[10\bar{1}0\right]$ at 1000K, in addition to other relative variations of E^* it presumes an anisotropic effect of the temperature on the elastic properties. A similar trend applies for F_y for which relative variations with temperature are strongly related to orientation. In the plastic regime, load drops are also slightly softer as marked by lower-amplitude force variations that are attributed to more spread nucleation events assisted by temperature.

Temperature also influences the elementary deformation processes. In general, decreasing the temperature leads to higher yield strength. In FCC metals, it is known that such stress increases at low temperature enhances dislocation dissociation and twinning[62,63]. A similar trend is observed in our simulations. Indeed, nanocompression normal to the $\{1\bar{2}10\}$ plane show partial dislocations in a pyramidal slip plane at 5K while only perfect one in the same slip plane are noticed at 1000

TABLE III. Elementary plasticity processes occuring in α-Al_2O_3 NPs under compression at T=5 and 1000 K as function of CA.

CA	5K	1000K
c	*R* twinning	*R* twinning
a	Pyramidal *n* slip (perfects + partials)	Pyramidal *n* slip (perfect)* + *c* slip
m	*c* and *R* slip (partials)	*c* slip (partials)
R	*c* and pyramidal slip (partials)	*c* slip (partials)

K. Furthermore, *c* and *R* slip are observed for CA normal to $(10\bar{1}0)$ plane as well as basal *c* and pyramidal slip for CA normal to $(10\bar{1}2)$ at 5 K while only *c* slip is shown at 1000 K for both orientations, see Table III. This effect of temperature on the plastic deformation of alumina is very similar to what is know in the case of bulk alumina[15,19,20]. This is illustrated in the work of Lagerlof and collaborators on bulk alumina where one can observe the effect of T on the critical resolve shear stress that becomes more favourable to basal slip at high-temperature[19], in a similar way that what is observed in our simulations.

Overall, MD nanocompression simulations performed using the Vashishta interatomic potentials allow to provide a detailed description of the influence of orientation and temperature on the mechanical properties and elementary deformation processes that control the plastic deformation of α-alumina at small-scale. These simulations when applied to α-Al_2O_3 NPs are particularly coherent with micro and bulk experiments and provide solid foundations to interpret future nanomechanical experiments as those performed *in situ* inside the TEM or in the SEM. In addition, they might have a direct impact on fabrication processes of nanocrystalline ceramics such as compaction or ball milling. Indeed, knowing the mechanical properties of NPs *i.e.,* the basic powder brick, and their orientation and temperature dependence could help to optimize processing conditions (pressure, temperature, *etc.*) opening new routes to deformable ceramics.

V. CONCLUSION

After the *in silico* design of neutral α-Al_2O_3 NPs, MD simulation was used to model nanocompression tests and investigate the deformation of alumina nanospheres as function of orientations and temperatures. Four directions were investigated with compression axis normal to *c*, *m*, *a* and

R planes. The mechanical response is characterized by elastic and plastic behaviours without failure during loading. The highest yield strength was noticed for CA normal to the *c* plane. At T=1000 K, both yield forces F_y and effective Young's modulus drop down whatever CA. The main deformation processes were investigated and a particular influence of the orientation was noticed including various dislocation and twinning processes when changing CA. At low temperature, *c*, *R* and pyramidal *n* slips were particularly observed, as well *R* twinning. Preliminary tests performed at higher temperature also demonstrated more favourable *c* slip and an anisotropic influence of the temperature on the elastic response of the NPs. These results help to interpret recent micropillar experiments and original deformation tests performed in bulk conditions and the model presented provides a rigourous theoretical background. In the future, these simulations and models could be used to better interpret TEM or SEM compression experiments applied to alumina providing direct evidences and theoretical justifications for temperature and orientation-dependent slip activity.

ACKNOWLEDGMENTS

Dr Q. Xu was the recipient of a PhD fellowship of the Chinese Scholarship Council (CSC). The authors are grateful to the Fédération Lyonnaise de Modélisation et Sciences Numériques (FLMSN) partner of the EQUIPEX EQUIP@MESO that provides the HPC resources.

DATA AVAILABILITY STATEMENT

All data that support the findings of this study are included within the article (and any supplementary files).

REFERENCES

[1] Webster TJ, Ergun C, Doremus RH, Siegel RW, Bizios R. Enhanced functions of osteoblasts on nanophase ceramics. Biomaterials. 2000;21(17):1803–1810.

[2] Chevalier J, Gremillard L. Ceramics for medical applications: A picture for the next 20 years. Journal of the European Ceramic Society. 2009;29(7):1245–1255.

[3] Wang Y, Jiang S, Wang M, Wang S, Xiao TD, Strutt PR. Abrasive wear characteristics of plasma sprayed nanostructured alumina/titania coatings. Wear. 2000;237(2):176–185.

[4]Nie X, Meletis E, Jiang J, Leyland A, Yerokhin A, Matthews A. Abrasive wear/corrosion properties and TEM analysis of Al_2O_3 coatings fabricated using plasma electrolysis. Surface and Coatings Technology. 2002;149(2-3):245–251.

[5]Knözinger H, Ratnasamy P. Catalytic aluminas: surface models and characterization of surface sites. Catalysis Reviews Science and Engineering. 1978;17(1):31–70.

[6]Manasilp A, Gulari E. Selective CO oxidation over Pt/alumina catalysts for fuel cell applications. Applied Catalysis B: Environmental. 2002;37(1):17–25.

[7]Sharifi EM, Karimzadeh F, Enayati M. A study on mechanochemical behavior of B_2O_3-Al system to produce alumina-based nanocomposite. Journal of Alloys and Compounds. 2009;482(1-2):110–113.

[8]Korte S, Clegg W. Discussion of the dependence of the effect of size on the yield stress in hard materials studied by microcompression of MgO. Philosophical Magazine. 2011;91(7-9):1150–1162.

[9]Korte S, Ritter M, Jiao c, Midgley P, Clegg W. Three-dimensional electron backscattered diffraction analysis of deformation in MgO micropillars. Acta Materialia. 2011;59(19):7241–7254.

[10]Du Z, Zeng XM, Liu Q, Lai A, Amini S, Miserez A, et al. Size effects and shape memory properties in ZrO_2 ceramic micro- and nano-pillars. Scripta Materialia. 2015;101:40–43.

[11]Amodeo J, Merkel S, Tromas C, Carrez P, Korte-Kerzel S, Cordier P, et al. Dislocations and plastic deformation in MgO crystals: a review. Crystals. 2018;8(6):240.

[12]Issa I, Joly-Pottuz L, Amodeo J, Dunstan DJ, Esnouf C, Réthoré J, et al. From dislocation nucleation to dislocation multiplication in ceramic nanoparticle. Materials Research Letters. 2021;9(6):278–283.

[13]Chen S, Liu F, Liu B, Chen X, Ke X, Zhang M, et al. Reaching near-theoretical strength by achieving quasi-homogenous surface dislocation nucleation in MgO particles. Materials Today. 2022;(55):37–45.

[14]Heuer A. Deformation twinning in corundum. The Philosophical Magazine: A Journal of Theoretical Experimental and Applied Physics. 1966;13(122):379–393.

[15]Castaing J, Cadoz J, Kirby S. Deformation of Al_2O_3 single crystals between 25°C and 1800°C: basal and prismatic slip. Le Journal de Physique Colloques. 1981;42(C3):C3–43.

[16]Cadoz J, Castaing J, Phillips D, Heuer A, Mitchell T. Work hardening and recovery in sapphire (α-Al_2O_3) undergoing prism plane deformation. Acta Metallurgica. 1982;30(12):2205–2218.

[17] Lagerlöf KPD, Pletka B, Mitchell T, Heuer A. Deformation and diffusion in sapphire (α-Al_2O_3). Radiation Effects. 1983;74(1-4):87–107.

[18] Cadoz J, Rivière J, Castaing J. TEM Observations of Dislocations in Al_2O_3 after Prism Plane Slip at Low Temperature under Hydrostatic Pressure. In: Deformation of ceramic Materials II. Springer; 1984. p. 213–222.

[19] Lagerlöf KPD, Heuer AH, Castaing J, Rivière JP, Mitchell TE. Slip and twinning in sapphire (α-Al_2O_3). Journal of the American Ceramic Society. 1994;77(2):385–397.

[20] Heuer A, Lagerlöf K, Castaing J. Slip and twinning dislocations in sapphire (α-Al_2O_3). Philosophical Magazine A. 1998;78(3):747–763.

[21] Castaing J, Munoz A, Garcia DG, Rodriguez AD. Basal slip in sapphire (α-Al_2O_3). Materials Science and Engineering: A. 1997;233(1-2):121–125.

[22] Lagerlöf K, Castaing J, Pirouz P, Heuer A. Nucleation and growth of deformation twins: a perspective based on the double-cross-slip mechanism of deformation twinning. Philosophical Magazine A. 2002;82(15):2841–2854.

[23] Castaing J, He A, Lagerlöf K, Heuer A. Deformation of sapphire (α-Al_2O_3) by basal slip and basal twinning below 700°C. Philosophical Magazine. 2004;84(11):1113–1125.

[24] Heuer A, Jia C, Lagerlöf K. The core structure of basal dislocations in deformed sapphire (α-Al_2O_3). Science. 2010;330(6008):1227–1231.

[25] Lagerlöf P. Crystal Dislocations: Their Impact on Physical Properties of Crystals. Multidisciplinary Digital Publishing Institute; 2018.

[26] Snow J, Heuer A. Slip systems in Al_2O_3. Journal of the American Ceramic Society. 1973;56(3):153–157.

[27] Geipel T, Lagerlöf K, Pirouz P, Heuer A. A zonal dislocation mechanism for rhombohedral twinning in sapphire (α-Al_2O_3). Acta Metallurgica et Materialia. 1994;42(4):1367–1372.

[28] He A, Lagerlöf KPD, Castaing J, Heuer AH. Considerations of the double-cross-slip mechanism for basal and rhombohedral twinning in sapphire (α-Al_2O_3). Philosophical Magazine A. 2002;82(15):2855–2867.

[29] Bodur C, chang J, Argon A. Molecular dynamics simulations of basal and pyramidal system edge dislocations in sapphire. Journal of the European ceramic Society. 2005;25(8):1431–1439.

[30] Shibata N, Chisholm M, Nakamura A, Pennycook S, Yamamoto T, Ikuhara Y. Nonstoichiometric dislocation cores in α-alumina. Science. 2007;316(5821):82–85.

[31] Kronberg M. Plastic deformation of single crystals of sapphire: basal slip and twinning. Acta Metallurgica. 1957;5(9):507–524.

[32] Bilde-Sørensen J, Lawlor B, Geipel T, Pirouz P, Heuer A, Lagerlöf K, et al. On basal slip and basal twinning in sapphire (α-Al_2O_3)—I. Basal slip revisited. Acta Materialia. 1996;44(5):2145–2152.

[33] Tsuruta K, Tochigi E, Kezuka Y, Takata K, Shibata N, Nakamura A, et al. Core structure and dissociation energetics of basal edge dislocation in α-Al_2O_3: A combined atomistic simulation and transmission electron microscopy analysis. Acta Materialia. 2014;65:76–84.

[34] Xu Q, Salles N, Chevalier J, Amodeo J. Atomistic simulation and interatomic potential comparison in α-Al_2O_3: lattice, surface and extended-defects properties. Modelling and Simulation in Materials Science and Engineering. 2022;30(3):035008.

[35] Montagne A, Pathak S, Maeder X, Michler J. Plasticity and fracture of sapphire at room temperature: Load-controlled microcompression of four different orientations. Ceramics International. 2014;40(1):2083–2090.

[36] Calvié E, Joly-Pottuz L, Esnouf C, Clément P, Garnier V, Chevalier J, et al. Real time TEM observation of alumina ceramic nano-particles during compression. Journal of the European Ceramic Society. 2012;32(10):2067–2071.

[37] Calvié E, Réthoré J, Joly-Pottuz L, Meille S, Chevalier J, Garnier V, et al. Mechanical behavior law of ceramic nanoparticles from transmission electron microscopy in situ nano-compression tests. Materials Letters. 2014;119:107–110.

[38] Thompson AP, Aktulga HM, Berger R, Bolintineanu DS, Brown WM, Crozier PS, et al. LAMMPS - a flexible simulation tool for particle-based materials modeling at the atomic, meso, and continuum scales. Computer Physics Communications. 2022;271:108171.

[39] Vashishta P, Kalia RK, Nakano A, Rino JP. Interaction potentials for alumina and molecular dynamics simulations of amorphous and liquid alumina. Journal of Applied Physics. 2008;103(8):083504.

[40] Nosé S. A unified formulation of the constant temperature molecular dynamics methods. The Journal of chemical physics. 1984;81(1):511–519.

[41] Issa I, Amodeo J, Réthoré J, Joly-Pottuz L, Esnouf C, Morthomas J, et al. In situ investigation of MgO nanocube deformation at room temperature. Acta Materialia. 2015;86:295–304.

[42] Amodeo J, Lizoul K. Mechanical properties and dislocation nucleation in nanocrystals with blunt edges. Materials and Design. 2017;135:223–231.

[43]Iteney H, Cornelius TW, Thomas O, Amodeo J. Load versus displacement-controlled nanocompression: Insights from atomistic simulations. Scripta Materialia. 2023;226:115245.

[44]Stukowski A. Visualization and analysis of atomistic simulation data with OVITO–the Open Visualization Tool. Modelling and simulation in materials science and engineering. 2009;18(1):015012.

[45]Stukowski A, Albe K. Extracting dislocations and non-dislocation crystal defects from atomistic simulation data. Modelling and Simulation in Materials Science and Engineering. 2010;18(8):085001.

[46]Lee W, Lagerlöf K. Structural and electron diffraction data for sapphire (α-Al_2O_3). Journal of Electron Microscopy Technique. 1985;2(3):247–258.

[47]Alpert CP, Chan HM, Bennison SJ, Lawn B. Temperature dependence of hardness of alumina-based ceramics. Journal of the American Ceramic Society. 1988;71(8):C–371.

[48]Vasylkiv O, Sakka Y, Skorokhod VV. Low-temperature processing and mechanical properties of zirconia and zirconia–alumina nanoceramics. Journal of the American Ceramic Society. 2003;86(2):299–304.

[49]Balla VK, Bose S, Bandyopadhyay A. Processing of bulk alumina ceramics using laser engineered net shaping. International Journal of Applied Ceramic Technology. 2008;5(3):234–242.

[50]Amodeo J, Pizzagalli L. Modeling the mechanical properties of nanoparticles: a review. Comptes Rendus Physique. 2021;22(S3):1–32.

[51]Bian JJ, Wang GF. Atomistic deformation mechanisms in copper nanoparticles. Journal of Computational and Theoretical Nanoscience. 2013;10(9):2299–2303.

[52]Kuksin AY, Yanilkin A. Formation of twins in sapphire under shock wave loading: atomistic simulations. Journal of Applied Physics. 2012;111(3):033513.

[53]Zhang C, Kalia RK, Nakano A, Vashishta P, Branicio PS. Deformation mechanisms and damage in α-alumina under hypervelocity impact loading. Journal of Applied Physics. 2008;103(8):083508.

[54]Bel Haj Salah S, Gerard C, Pizzagalli L. Influence of surface atomic structure on the mechanical response of aluminum nanospheres under compression. Computational Materials Science. 2017 03;129:273 – 278.

[55]Goryaeva AM, Fusco C, Bugnet M, Amodeo J. Influence of an amorphous surface layer on the mechanical properties of metallic nanoparticles under compression. Physical Review Materials. 2019;3(3):033606.

[56] Amodeo J, Bitzek E, Begau C. Atomistic Simulations of Compression Tests on Ni_3Al Nanocubes. Materials Research Letters. 2014 07;2(3):140 – 145.

[57] Zhang W, Gao Y, Xia Y, Bei H. Indentation Schmid factor and incipient plasticity by nanoindentation pop-in tests in hexagonal close-packed single crystals. Acta Materialia. 2017;134:53–65.

[58] Sarobol P, Chandross M, Carroll JD, Mook WM, Bufford DC, Boyce BL, et al. Room temperature deformation mechanisms of alumina particles observed from in situ micro-compression and atomistic simulations. Journal of Thermal Spray Technology. 2016;25(1-2):82–93.

[59] Kim HT. High thermal conductivity ceramics and their composites for thermal management of integrated electronic packaging. Heat Transfer-Models, Methods and Applications. 2018:333–359.

[60] Lin J, Jiang F, Xu X, Lu J, Tian Z, Wen Q, et al. Molecular dynamics simulation of nanoindentation on c-plane sapphire. Mechanics of Materials. 2021;154:103716.

[61] Kim WK, Xi D, Kim BH. Nanoscale indentation and scratching tests of single crystal sapphire using molecular dynamics simulation. Computational Materials Science. 2019;170:109195.

[62] El-Danaf E, Kalidindi SR, Doherty RD. Influence of grain size and stacking-fault energy on deformation twinning in fcc metals. Metallurgical and Materials Transactions A. 1999;30(5):1223–1233.

[63] Ogata S, Li J, Yip S. Energy landscape of deformation twinning in bcc and fcc metals. Physical Review B. 2005;71(22):224102.

LIST OF CAPTIONS

Fig. 1 Pattern-based method to construct α-Al_2O_3 neutral NPs. (a) α-Al_2O_3 partial unit cell with identification of the two motives to pattern, (b) x and z projections of both molecular motives, (c) 3D canvas made of replicated motives 1 and 2 from which the neutral nanosphere is carved out.

Fig. 2 α-Al_2O_3 hexagonal cell outlines and main crystallographic slip planes.

Fig. 3 Force *vs.* displacement curves for α-Al_2O_3 nanospheres under compression with compression axis normal to the (a) c, (b) a, (c) m and (d) R planes. Blue, black and red solid curves refer respectively to NP diameter D=7.2, 10.0 and 15.2 nm. The Hertz model is shown using dashed curves. Simulations are performed at T=5 K (thin curves) for the three diameter sizes except for D=15.2 nm for which additional T=1000 K data (thicker curves) are shown. For this latter, raw data are shown blurred while a Bezier fit is highlighted.

Fig. 4 Nucleation of rhombohedral twins in a 15.2 nm α-Al_2O_3 NP under compression along the c plane. Displacements (a) δ=17.5 Å, (b) δ=27.0 Å and (c) δ=27.1 Å are shown. An angle of 58° is measured between the first twinning plane and the c plane. Nanoparticle cross-sections are illustrated with (back figures) and without (front figures) perfect crystal atoms to emphasize the presence of defects. Only O atoms are shown for the sake of clarity. They are colored in red or light-grey depending on the local crystal structure *i.e.,* respectively when they belong to the HCP perfect crystal environment or defective regions (surfaces or twin boundaries). Grain and twin boundary interfaces are colored in yellow. In the top-right inset, both O and Al atom sublattices are shown respectively in blue and red.

Fig. 5 Compression of α-Al_2O_3 NPs normal to the prism *a* plane. (a) δ=9.1 Å, nucleation and propagation of a perfect $(11\bar{2}3)$ pyramidal dislocation, (b) δ=13.7 Å, formation of a triangular structure made of perfect dislocations gliding in $(11\bar{2}3)$ and $(2\bar{1}\bar{1}3)$. (c) δ=16.3 Å, the triangular dislocation structure fails and partial dislocations multiply within same pyramidal slip planes. Staking-faults are emphasized using yellow interfaces in the main figure, light-grey one in the inset. (d) δ=16.4 Å, the accumulation of closed stacking-faults in the pyramidal planes lead to structural change in the central part of the NP. Additional information are provided in the caption of the Figure 4. In addition, the local crystallographic structure of the transformed domain is illustrated in the inset, perfect dislocations are shown in green while Burgers vectors are shown using blue arrows.

Fig. 6 Compression of α-Al_2O_3 NPs normal to the prism *m* plane. (a) up to δ=0.1 Å, the NP rotates to accommodate the deformation and the basal plane is tilted of about 3° from CA, (b) δ=12.9 Å, basal partial dislocations nucleate from the contact region with the indenter. Dislocations colored in orange refer to $\frac{1}{3}[10\bar{1}0]$ dislocations (atoms colored in green rely to the stacking-faults). (c) δ=17.5 Å, dislocations nucleate in the rhombohedral $(1\bar{1}02)$ slip system at 65° from the compression axis and interact with basal dislocations. Additional information are provided in the caption of the Figure 4.

Fig. 7 Compression of α-Al_2O_3 NP with CA normal to a rhombohedral *R* plane. (a) δ=11.9 Å, nucleation of dissociated dislocations in the *c* plane. Partial dislocations are colored in orange, stacking fault atoms in green, (b) δ=18.2 Å, basal (colored in orange) and pyramidal (colored in green) dislocations nucleating and propagating, (c) δ=30.0 Å, basal partial dislocations gliding in planes close to transformed domains associated to the propagation of pyramidal *n* partial dislocations (stacking-fault atoms colored in blue). Additional information are provided in the caption of the Figure 4.

Fig. 8 Stacking-fault energy (SFE) profiles in *c*, *a*, *m*, *n*, *s* and *R* slip planes computed using the Vashishta interatomic potentials. Profile directions corresponding to Burgers vectors are provided in the legend.

Tab. 1 Mechanical response of α-Al_2O_3 nanosphere under compression as function of orientation (CA) and size (D) at T=5 K. Effective Young's modulus E^*, fitting intervals $[E^*]$ and critical data for dislocation or twin nucleation including critical force F_c, displacement δ_c and strain ε_c. Additional data for T=1000 K are shown between braces for D=15.2 nm NPs.

Tab. 2 Schmid factor analysis as function of compression orientation and slip system in α-Al_2O_3. $\vec{b_p}$ refers for (leading or trailing) partial dislocation Burgers vector while $\vec{b}$ relies on perfect Burgers vectors. M and M_p refer respectively to perfect and partial systems Schmid factors.

Tab. 3 Elementary plasticity processes occuring in α-Al_2O_3 NPs under compression at T=5 and 1000 K as function of CA.